Joule

CellPress
OPEN ACCESS

Article

A polymer bilayer hole transporting layer architecture for high-efficiency and stable organic solar cells

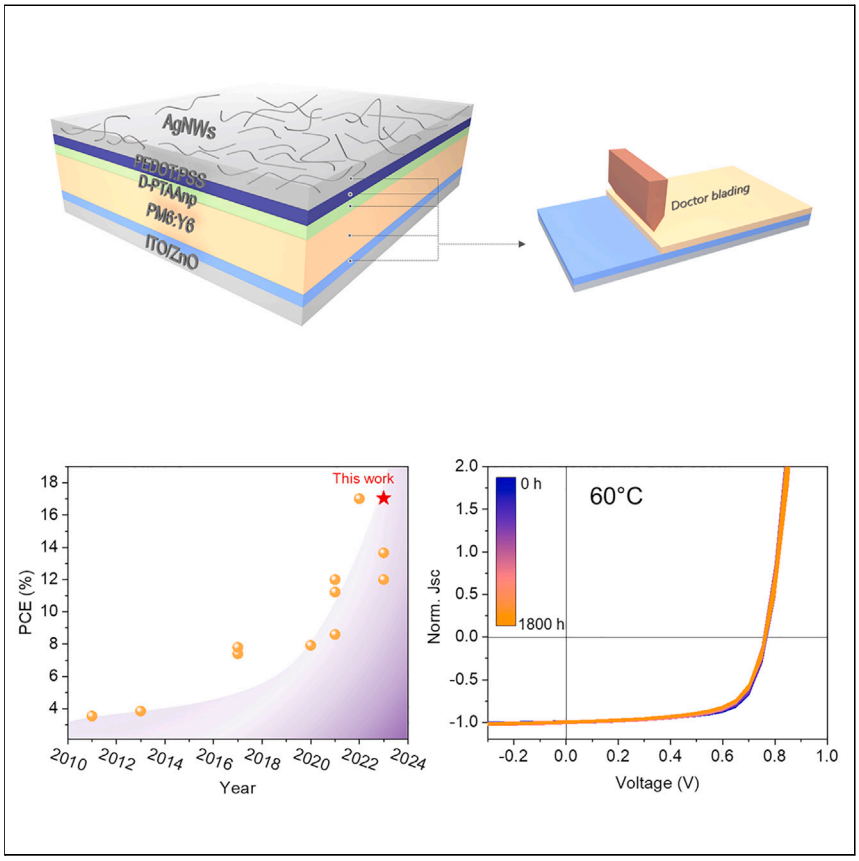

Two major bottlenecks for organic photovoltaic module production are device stability and the development of an architecture that allows using the newest high-efficiency active layer materials in large-scale solution-based processing. A concept for novel interface layers is presented that combines compatibility for high-efficiency active layer materials in state-of-the-art solution processing with exceptional operational stability. Doped nanoparticles enable tuning of electrical properties as well as processing of organic polymers on top of the active layer.

Junyi Xu, Thomas Heumüller, Vincent M. Le Corre, ..., Johannes Frisch, Marcus Bär, Christoph J. Brabec

junyi.xu@fau.de (J.X.)
thomas.heumueller@fau.de (T.H.)
christoph.brabec@fau.de (C.J.B.)

Highlights

A bilayer HTL strategy is developed for efficient non-fullerene OPV cells

A PCE of 17.1% was reported for inverted OPV cells with solution-processed HTL

The bilayer HTL strategy enhances the operational stability of OPV cells

Xu et al., Joule 8, 2570–2584
September 18, 2024
Published by Elsevier Inc.
https://doi.org/10.1016/j.joule.2024.06.013

CellPress
OPEN ACCESS

Joule

Article

A polymer bilayer hole transporting layer architecture for high-efficiency and stable organic solar cells

Junyi Xu,[1,*] Thomas Heumüller,[1,2,7,*] Vincent M. Le Corre,[1,2] Anastasiia Barabash,[1] Roberto Félix,[3] Johannes Frisch,[3] Marcus Bär,[3,4,5,6] and Christoph J. Brabec[1,2,*]

SUMMARY

All-solution-processed organic photovoltaic (OPV) cells allow cost- and energy-effective fabrication methods for large-area devices. Despite significant progress on laboratory-scale devices, there is still a lack of interface materials that can be solution processed on top of the active layer, are compatible with novel non-fullerene acceptors (NFAs), and also provide sufficient long-term stability. We developed a novel interface layer concept, where alcohol-based organic polymer nanoparticles can be processed on top of a polymer-NFA active layer and doped to achieve a quasi-Ohmic hole contact. Moreover, poly(3,4-ethylenedioxythiophene):poly(styrenesulfonate) (PEDOT:PSS) is processed as a second layer, forming a bilayer solution-processed hole transporting layer (HTL), providing an industrially relevant inverted architecture with a protective PEDOT:PSS layer on top. Most importantly, exceptional stability is observed. PM6:Y6 devices with the bilayer HTL are demonstrated to maintain 93% of their initial efficiency for 1,800 h under continuous solar cell operation at 60°C.

INTRODUCTION

Organic photovoltaic (OPV) cells have emerged as an exciting class of renewable energy devices. They can be used as a power source, allowing for seamless integration into buildings or internet of things (IoT) platforms, where weight, flexibility, and/or semi-transparency are key requirements.[1–3] Moreover, the solution processability of OPVs enables cost-efficient, high-throughput printing production by roll-to-roll (R2R) techniques, with some large-area examples reaching certified power conversion efficiencies (PCE) of up to 12.6% (11.7%) on 26 cm^2 (204 cm^2).[4] Over the past decade, the development of non-fullerene acceptors (NFAs) has pushed PCE to a level sufficient for widespread applications.[5–9]

To commercialize the OPV technology, excellent stability (including light and thermal stability) is required to guarantee long-term operation in indoor as well as outdoor environments. Proper encapsulation can protect from extrinsic degradation caused by oxygen, water, and mechanical stress. However, this still requires a sufficient intrinsic OPV stability. Both burn-in (i.e., the initial period of steep degradation) and long-term degradation phenomena were observed for encapsulated OPVs.[10] Kinetics- and thermodynamics-induced morphology change (aggregation, phase separation) has been identified as one degradation pathway of organic solar cells.[11] Morphological instability is typically accelerated under thermal stress.[12] Several strategies, mainly addressing the thermodynamic instability of non-equilibrium

CONTEXT & SCALE

Organic photovoltaic (OPV) devices achieve close to 20% efficiency, and high intrinsic light stability of a few active layer materials has been reported under concentrated conditions, raising the expectations for long-term stable products. Nevertheless, currently no high-efficiency (>10%) OPV module with long-term stability is commercially available. A major bottleneck for OPV stability is the interface layers. Most large-area OPV modules rely on an inverted architecture with a thick PEDOT:PSS interface layer on top to protect the active layer from processing solvents in electrode materials and encapsulation glues. Although those architectures work well for fullerene-based systems, severe stability limitations have arisen with high-efficiency non-fullerene acceptors (NFAs). We present a novel hole-transport-layer concept that provides exceptional stability for devices with high-efficiency NFA materials in an industrially relevant inverted architecture including a PEDOT:PSS top layer.

active layers, have been proposed to improve stability. For instance, burn-in free devices have been demonstrated by replacing fullerene with NFAs,[13,14] and the photo-induced energetic disorder can be suppressed when using more ordered materials.[15,16] Morphological-related instability can be resolved by identifying compatible donor and acceptor compounds within a molecular interaction-diffusion framework.[17] Ternary and all polymer blend concepts are used to better control molecular interactions and suppress phase separation.[18–21] With a better understanding of the degradation mechanism of NFA-based devices, some newly developed composites have shown a lower tendency for diffusion, thus improving the morphological stability.[22,23]

Industrially solution-processed OPV modules rely on the inverted architecture with a several 100 nm thick and robust poly(3,4-ethylenedioxythiophene):poly(styrenesulfonate) (PEDOT:PSS) interface layer to protect the semiconductor during top electrode printing. This has been considered the baseline process for fullerene-based composites,[24–26] as PEDOT:PSS provides good selectivity to and negligible reactivity with fullerenes. This has changed with the replacement of fullerenes by NFAs. Only few NFAs were reported to provide a high PCE with PEDOT:PSS, while most of the high performance NFAs required an evaporated molybdenum oxide (ev-MoO_x) electrode.[13] Obviously, the material's strategy for solution-processed hole transporting layers (HTLs) being generically compatible with NFAs devices is lagging far behind. The commonly used aqueous solution-processed PEDOT:PSS has difficulties to result in a uniform film on top of the hydrophobic active layer surface. The wetting issue can be addressed by adding surfactants into the PEDOT:PSS; however, many of the surfactants show adverse side reactions with NFAs, leading to a performance reduction as compared with ev-MoO_x interface layers. Alcohol-based metal-oxide nanoparticles suffer from poor long-term stability due to the high density of defects and photocatalytic effect.[27] Metal-oxide nanoparticles are also prone to pinhole formation during film coating, leading to device shunting. Thus, with an ultimate goal of commercializing all-solution-processed OPVs, stable and robust HTLs that can also be processed from solutions are urgently needed.

A breakthrough was recently reported for a PSS free PEDOT (PEDOT:F), where the acidic PSS was replaced by a fluorinated dopant (perfluorinated sulfonic acid ionomers).[28] PEDOT:F was demonstrated to give high performance as well as decent stability with various NFA systems and was moreover demonstrated to be compatible with solution-processed silver nanowires (AgNWs) top electrodes.[29]

Here, we introduce a novel device architecture for highly efficient and stable NFA-based OPV cells that is capable to operate with conventional acidic PEDOT:PSS in a solution-processed polymer bilayer as HTL. The bilayer HTL is composed of doped poly[bis(4-phenyl)(2,5,6-trimethylphenyl)amine (PTAA) nanoparticles (prepared according to our recently published method[30]) and PEDOT:PSS without any further surfactants. Doped PTAA nanoparticles (D-PTAAnp) serve as a buffer layer, provide proper alignment of the hole transport levels, and enable efficient hole extraction, while PEDOT:PSS forms a dense layer, protecting the active layer and furthermore enabling Ohmic contact to the Ag electrode. As a result, we fabricated inverted OPV cells with PCE of 17.1%, which is, to the best of our knowledge, among the highest reported efficiencies for inverted OPV cells using PEDOT:PSS as HTL. Our devices also exhibit excellent operational stability and retain 95% of their initial performance after 1,600 h operating under metal-halide lamp illumination at room temperature (RT) and 93% of their initial performance after 1,800 h operating under metal-halide lamp illumination at 60°C. We extend this bilayer architecture to the state-of-the-art NFA systems and demonstrate universality.

[1]Institute of Materials for Electronics and Energy Technology (i-MEET), Department of Materials Science and Engineering, Friedrich-Alexander-Universität Erlangen-Nürnberg (FAU), Martensstrasse 7, 91058 Erlangen, Germany

[2]Helmholtz Institute Erlangen-Nürnberg for Renewable Energy (HI ERN), Immerwahrstrasse 2, 91058 Erlangen, Germany

[3]Department of Interface Design, Helmholtz-Zentrum Berlin für Materialien und Energie GmbH, Albert-Einstein-Strasse 15, 12489 Berlin, Germany

[4]Energy Materials In-situ Laboratory Berlin (EMIL), Helmholtz-Zentrum Berlin für Materialien und Energie GmbH, Albert-Einstein-Strasse 15, 12489 Berlin, Germany

[5]Helmholtz Institute Erlangen-Nürnberg for Renewable Energy (HIERN), Albert-Einstein-Strasse 15, 12489 Berlin, Germany

[6]Department of Chemistry and Pharmacy, Friedrich-Alexander-Universität Erlangen-Nürnberg (FAU), Egerlandstrasse 3, 91058 Erlangen, Germany

[7]Lead contact

*Correspondence: junyi.xu@fau.de (J.X.), thomas.heumueller@fau.de (T.H.), christoph.brabec@fau.de (C.J.B.)

https://doi.org/10.1016/j.joule.2024.06.013

Finally, all-solution-processed OPV cells with Ag nanowire electrodes have demonstrated remarkable stability as well.

RESULTS AND DISCUSSION

Architecture and photovoltaic performance of bilayer HTL-based devices

Despite the potential advantages of PEDOT:PSS as a solution-processed HTL material in organic solar cells, the inverted devices with PEDOT:PSS on top of the active layer always show a low open-circuit voltage (V_{oc}) due to the energy-level misalignment at the active layer/PEDOT:PSS interface.[31] Surfactants, required to improve the wettability of PEDOT:PSS, are also adverse to the device efficiency and stability. To overcome these problems, we introduce a polymer bilayer architecture composed of a D-PTAAnp layer below a PEDOT:PSS (see scheme in Figure 1G). We briefly rationalize this very specific material design and refer to a recent publication providing all the details on the synthesis and functionality of doped organic semiconducting nanoparticles.[30] First, to prevent dissolving the bulk-heterojunction layer, we searched for concepts to process PTAA from alcohols. Following our previous work on organic semiconducting nanoparticles, we succeeded in developing a ligand-free PTAA-based dispersion in isopropanol with a simple ligand-free rapid precipitation process.[32] Second, and to maintain an overall low contact resistance, we decided to dope the nanoparticles with a Lewis acid dopant, tris(pentafluorophenyl)-borane, to provide sufficient conductivity but maintain mild doping conditions. The doping effect of PTAA is confirmed by UV-vis photometry measurements revealing the emergence of an additional polaron absorption band.[33] Third, to overcome the wetting and drying instabilities of aqueous PEDOT:PSS, we take advantage of the nanoparticular nature of the PTAAnp film, where the single nanoparticles are acting as anchoring points that effectively prevent de-wetting during the drying process. As expected, D-PTAAnp films show increased electrical conductivity as well as a larger work function (see Figures S1 and S3). Furthermore, the D-PTAAnp layer provided a large matrix of nanoparticular anchoring points, allowing for the coating of a continuous PEDOT:PSS layer on top of PM6:Y6 without any surfactant (Figures S4 and S5). The chemical structures of the PM6 and Y6 materials are depicted in Figure S6. Figures 1A and 1B show the scanning electron microscopy (SEM) top-view images of the active layer gradually covered by the bilayer HTL. The D-PTAA nanoparticles are perfectly sized (~50 nm, Figure S7) and dispersed forming a homogeneous structure in the nanometer domain. The PEDOT:PSS layer, sequentially coated from water on top of the D-PTAAnp layer, forms (without any additives) a dense and homogeneous film, a prerequisite for good electrical transport, stable operation, and reproducible manufacturing. The effect of the nanoparticles on the deposition of PEDOT:PSS was further investigated by atomic force microscopy (AFM). The pure nanoparticles layer exhibits a root mean square (RMS) surface roughness of around 17.24 nm, while the bilayer sample displays a smoother surface with a smaller RMS roughness of 5.20 nm (Figures 1E, 1F, and S8).

Figure 1H shows the J-V curves of control and bilayer devices under simulated AM 1.5 G solar irradiation (100 mW/cm^2). The key PV parameters are summarized in Table 1. The device based on PEDOT:PSS (with surfactant) gives a PCE of 7.19% with a short-circuit current density (J_{sc}) = 24.10 mA/cm^2, open-circuit voltage (V_{oc}) = 0.53 V, and fill factor (FF) = 56.5%. The bilayer device shows a PCE of 14.63% with J_{sc} = 24.44 mA/cm^2, V_{oc} = 0.83 V, and FF = 72.1%, which is comparable to the device with ev-MoO_x as HTL (Figure S9). Moreover, we find that the bilayer device has a lower series resistance than the PEDOT:PSS device (Figure S11). The lower series resistance in the bilayer device suggests enhanced charge transport

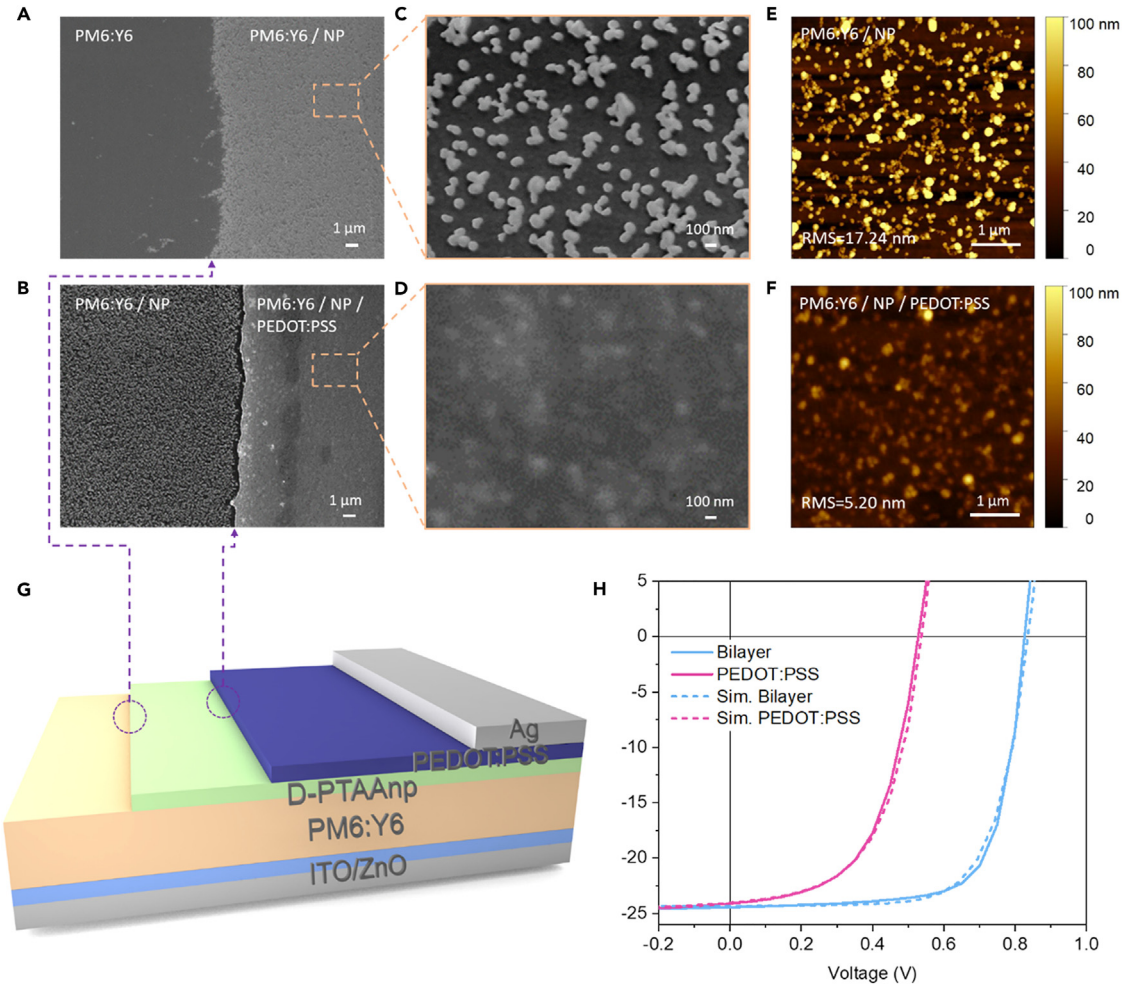

Figure 1. Architecture and properties of bilayer HTL-based OPV cells

(A and B) Top-view SEM images of intentionally partially covered (A) D-PTAAnp on PM6:Y6 active layer and (B) PEDOT:PSS on the PM6:Y6/D-PTAAnp layer.

(C and D) High-resolution SEM images of the area boxed in (A) and (B).

(E and F) AFM topographical images of the (E) PM6:Y6/D-PTAAnp layer and (F) PM6:Y6/D-PTAAnp/PEDOT:PSS layer.

(G) The structure of OPV cells based on the bilayer HTL.

(H) Experimental (solid lines) and simulated (dashed lines) J-V characteristics of OPV cells that feature either PEDOT:PSS only or D-PTAAnp/PEDOT:PSS bilayer HTL according to the structure described in (G). Simulations were performed by using a drift-diffusion model, and the parameters are presented in Table S2.

through the nanoparticle and PEDOT:PSS bilayer HTL, which accounts for the improved FF. We investigated different combinations of electron transporting layer (ETL) and PTAAnp modifications. It is notable that a PCE of 13.87% is achieved by undoped PTAAnp as a buffer layer (Table S1). We account that to the mesoscopic nature of the PTAAnp layer, where the electrical transport requirements are less demanding than for a thick and fully covering PTAA layer. Considering the practical side of production, we also replaced the ZnO sol-gel layer with a commercial ZnO NP dispersion. A very comparable performance and a PCE of 13.70% were found for this combination (Table 1). We further tested the photovoltaic performance of devices using solution-processed metal-oxide nanoparticles but always found clearly reduced PCE values of below 11% (Table S1). Therefore, our strategy of constructing a bilayer polymer HTL is considered to be effective in improving the interfacial contact between the active layer and PEDOT:PSS.

Table 1. Photovoltaic performance of OPV cells

Device	J_{sc} cal. (mA/cm^2)	J_{sc} (mA/cm^2)	V_{oc} (V)	FF (%)	PCE (%)
Bilayer[a]	24.13	24.44 (24.28 ± 0.16)	0.830 (0.827 ± 0.002)	72.1 (71.2 ± 0.8)	14.63 (14.30 ± 0.31)
Bilayer[b]	23.15	23.27 (23.12 ± 0.14)	0.831 (0.830 ± 0.001)	70.9 (70.6 ± 0.2)	13.70 (13.54 ± 0.15)
PEDOT:PSS[c]	24.04	24.10 (24.01 ± 0.08)	0.530 (0.520 ± 0.009)	56.3 (55.3 ± 0.9)	7.19 (6.90 ± 0.29)

[a]The device based on ZnO sol-gel.
[b]The device based on commercial ZnO nanoparticles.
[c]The device based on PEDOT:PSS mixed with surfactant. Note: average values with standard derivation were from over 6 devices.

Hole-injection enhancement in the bilayer HTL

The nature of the bilayer HTL is further investigated with J-V characteristics of hole-only devices. The energy-level alignment between PM6:Y6 and PEDOT:PSS, D-PTAAnp/PEDOT:PSS bilayer, and ev-MoO_x top HTLs was derived from the simulation of the hole-only device dark J-V curves. As can be seen in Figure 2B, the PEDOT:PSS-based device shows a stronger asymmetry and an overall reduced current density with the current injected from the top PEDOT:PSS being lower than the current injected from the bottom PEDOT:PSS. This is a clear sign of an asymmetric device structure with the PEDOT:PSS hole-only device having a significant built-in voltage (V_{BI}).[34] The current injected from the top electrode is improved by two orders of magnitude when inserting a D-PTAAnp in between the active layer and the PEDOT:PSS layer (i.e., when using the polymer bilayer HTL). The result is comparable to the cell with an ev-MoO_x top contact, which is the standard HTL in inverted OPV cells. The symmetric shape of the J-V curve further implies that we have a low V_{BI} and the formation of a quasi-Ohmic contact when using a D-PTAAnp/PEDOT:PSS bilayer HTL.

To validate this hypothesis, it should be verified that the injected currents are space charge limited by the semiconductor and not limited by the residual barrier at the interface. This is analyzed by means of the double-logarithmic J-V curves plotted in Figure 2C. For both the bilayer and ev-MoO_x-based devices, the experimental current yields a straight line with a slope of 2, indicating the injected current is indeed space charge limited by the semiconductor. These results underline the formation of a quasi-Ohmic hole contact in case D-PTAAnp is located between PM6:Y6 and PEDOT:PSS. The drift-diffusion simulations reveal further insight into the trap density of the bilayer structure. The trap density in the PEDOT:PSS device is 3.04×10^{16} cm^{-3}, while the trap density in the bilayer HTL device is lower than the simulation threshold (Table S3).[35] Furthermore, the simulations suggest that the highest occupied molecular orbital (HOMO) offset between the active layer and the HTL decreases from 0.41 eV for PEDOT:PSS to 0.23 eV for the D-PTAAnp/PEDOT:PSS bilayer. The large energy offset in the case of using a PEDOT:PSS HTL may indicate the presence of a significant injection barrier.

We explore this further by drift-diffusion simulations of light J-V curves of full solar cells. The shape of the experimental curves is well simulated as seen in Figure 1H. Simulation details are presented in Table S2. Notably, the solar cell with only PEDOT:PSS again shows a high density of traps, as also observed in the fitting of hole-only devices, while in both cases no traps are observed with the addition of a nanoparticle layer. The drift-diffusion simulations indicate that besides an injection barrier, also surface traps limit the PEDOT:PSS solar cell, while those traps are absent when using a D-PTAAnp layer.

To further explore the mechanism behind the improved device performance resulting from the incorporation of the D-PTAAnp layer between the PM6:Y6 active layer and PEDOT:PSS heterointerface, ultraviolet photoelectron spectroscopy (UPS)

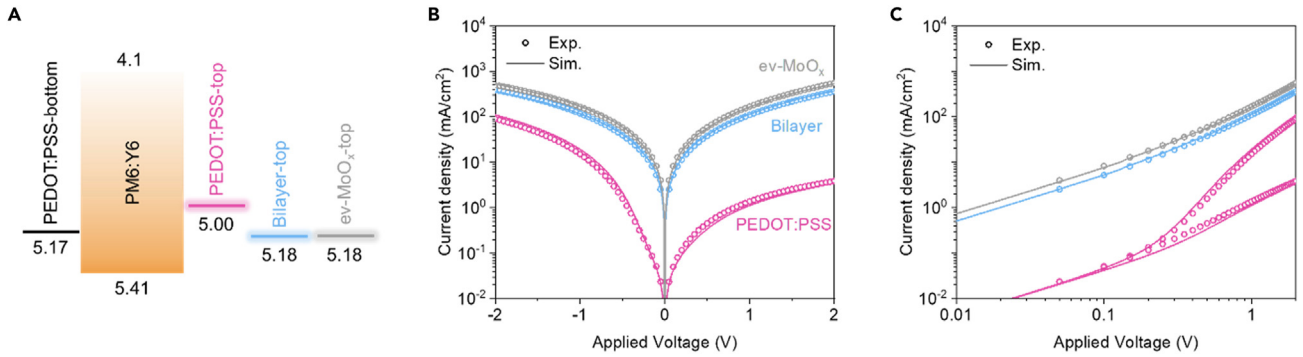

Figure 2. Hole-only devices

(A) Schematic energy-level position diagram of each layer in different hole-only devices with structures of indium tin oxide (ITO)/PEDOT:PSS/PM6:Y6/PEDOT:PSS/Ag (pink curve), ITO/PEDOT:PSS/PM6:Y6/bilayer/Ag (blue curve), and ITO/PEDOT:PSS/PM6:Y6/ev-MoO_x/Ag (gray curve). The energy levels are obtained from the simulation of experimentally derived dark J-V data using a drift-diffusion model.

(B) Experimental (circles) and simulated (solid lines) dark J-V characteristics of hole-only devices with different HTLs.

(C) Double-logarithmic presentation of the J-V characteristics of hole-only devices shown in (B). The symbols and lines of the devices represent the measured and simulated hole current under reverse and forward bias, respectively.

measurements were performed on PM6:Y6, PM6:Y6/PEDOT:PSS, and PM6:Y6/D-PTAAnp/PEDOT:PSS bilayer HTL samples. The secondary electron cutoff (SECO) region and the HOMO regions are presented in Figure S16. Summarily, work function (Φ) values of ~4.7 ($\pm$ 0.1) eV were determined for the three samples (see Figure S16A). The HOMO position of the PM6:Y6 was found to be (-0.4 ± 0.1) eV away from the Fermi (E_F) level, while the UPS spectra of the two samples with PEDOT:PSS top layers (i.e., with and without a D-PTAAnp layer) show band tails extending all the way to the E_F level (see Figures S16B and S16C), a well-known characteristic of PEDOT:PSS.[36]

Hence, while the absolute numbers of energy-level positions derived from simulations (see Figure 2A) and UPS measurements (see Figure S16D) differ, the UPS data corroborates the presence of a significant HOMO offset between the active layer and PEDOT:PSS and thus further validates the results of the drift-diffusion model used to simulate the J-V curves. However, the D-PTAAnp-induced decrease of this barrier, which had been revealed as another result of the J-V curve simulations, cannot be observed in the UPS data. However, this seeming contradiction can be explained by the inherent specifics of the two characterization approaches. Whereas the J-V characteristic will be affected by electronic structure changes throughout the device stack, which is simulated taking the energy-level offsets at the interfaces of the involved layers into account, the UPS measurements only probe the top surface (i.e., a few nanometers) of the studied layer stack samples (see experimental procedures section). Hence, the PM6:Y6/PEDOT:PSS interface that is supposed to be improved by the addition of the D-PTAAnp layer is buried too deeply to be probed by UPS, and thus deriving the same HOMO/SECO position for the PM6:Y6/PEDOT:PSS and the PM6:Y6/D-PTAAnp/PEDOT:PSS bilayer HTL samples is actually not surprising. The fact that UPS derives a similar HOMO offset between PM6:Y6 and PEDOT:PSS as is derived based on J-V curve simulations, however, suggests a homogeneous electronic structure profile throughout the PEDOT:PSS, presumably resulting in similar HOMO positions close to the PM6:Y6 active layer and at its surface. In light of the J-V curve simulation, which revealed a reduced injection barrier upon D-PTAAnp addition, finding a similar HOMO position for the surface of the PM6:Y6/D-PTAAnp/PEDOT:PSS bilayer HTL sample suggests the presence of a significant electronic structure profile throughout this layer stack.

To conclude, the addition of nanoparticles reduces the injection barrier at the buried PM6:Y6/PEDOT:PSS interface, resulting in improved energy-level alignment and improved device performance. The addition of D-PTAAnp thus results in a solution-processed HTL with a similar performance as the ev-MoO_x HTL that can be used in an inverted structure.

Device stability

Having established a reasonably performing baseline for D-PTAAnp/PEDOT:PSS bilayer HTL-based PM6:Y6 devices, we next turn the attention to the operational stability. In detail, we monitored the operational long-term stability of unencapsulated devices under illumination and in a N_2 atmosphere for the various HTLs combinations introduced above. We decided to use the commercial ZnO NP dispersion (see device data in Table 1) for the stability investigations to operate devices as close as possible to the commercial state of the art. The bilayer device maintained nearly 95% of its initial efficiency after 1,600 h of operation at RT (ISOS-L-1 protocol). The J-V curves before and after that operation period remained almost unchanged. By contrast, the device based on PEDOT:PSS started at lower absolute efficiencies, which further dropped to 70% of their initial values within 1,600 h due to a rapid decrease in FF (Figures 3A, 3B, and S17). Even the device based on ev-MoO_x underwent some degradation but maintained a decent stability of over 85% after degradation (see Figure S18). We want to highlight that these stability values were achieved for binary PM6:Y6 composites. Recent stable PM6:Y6 devices were reported for ternary composites,[18,29] where a third component was required to stabilize the microstructure. We also tested the operational stability of bilayer devices with metal-oxide nanoparticles (MoO_x, Ta-WO_x, and Sb-SnO_x) as a buffer layer, which has been reported to give an impressive efficiency.[37] All the metal-oxide nanoparticle-based devices exhibited short lifetimes (<100 h) because of a significant drop in V_{oc} and FF (Figures S20 and S21). Finally, we wanted to explore the stability limits of binary PM6:Y6 devices with the D-PTAAnp/PEDOT:PSS interlayer. In order to challenge the thermal stability of a binary microstructure, we applied the ISOS-L-2 protocol, where devices are tested at 60°C under illumination. To our surprise, the devices with the bilayer electrode did not show a significant accelerated degradation at 60°C. We find more or less identical stability values at RT and at 60°C. More than 94% of the initial PCE is maintained after operating our devices at 60°C after 1,800 h (Figures 3C and 3D). Statistical analysis of the device stability data reveals that the performance of the bilayer device is reproducible (Figures S22 and S23).

Universality of this approach

To demonstrate the universality of this interlayer, we selected four further organic semiconductor composites with various HOMO energy levels, including PM7:Y6, PTQ11:Y6, PM6:DT-Y6, and PM6:BTP-eC9:L8-BO. The molecular structures of the corresponding materials are shown in Figure 4A. The detailed photovoltaic parameters of the investigated devices are summarized in Table S4. All the systems based on a pristine PEDOT:PSS HTL showed poor photovoltaic performance with low V_{oc} and FF. By contrast, all the D-PTAAnp/PEDOT:PSS bilayer devices exhibited performance values comparable to the devices based on ev-MoO_x (Figure 4B). For instance, the PM6:BTP-eC9:L8-BO device based on the bilayer HTL achieved a PCE of 17.1%. To the best of our knowledge, this is among the highest efficiencies reported thus far for inverted OPV cells with solution-processed HTL, as depicted in Figure 4E. The integrated J_{sc} values from the measured external quantum efficiency (EQE) of all the devices are shown in Figure S25 and are well consistent to those obtained from the J-V curves. Interestingly, the EQE values of the bilayer devices are slightly higher compared with the ones with ev-MoO_x. Although the origin of this

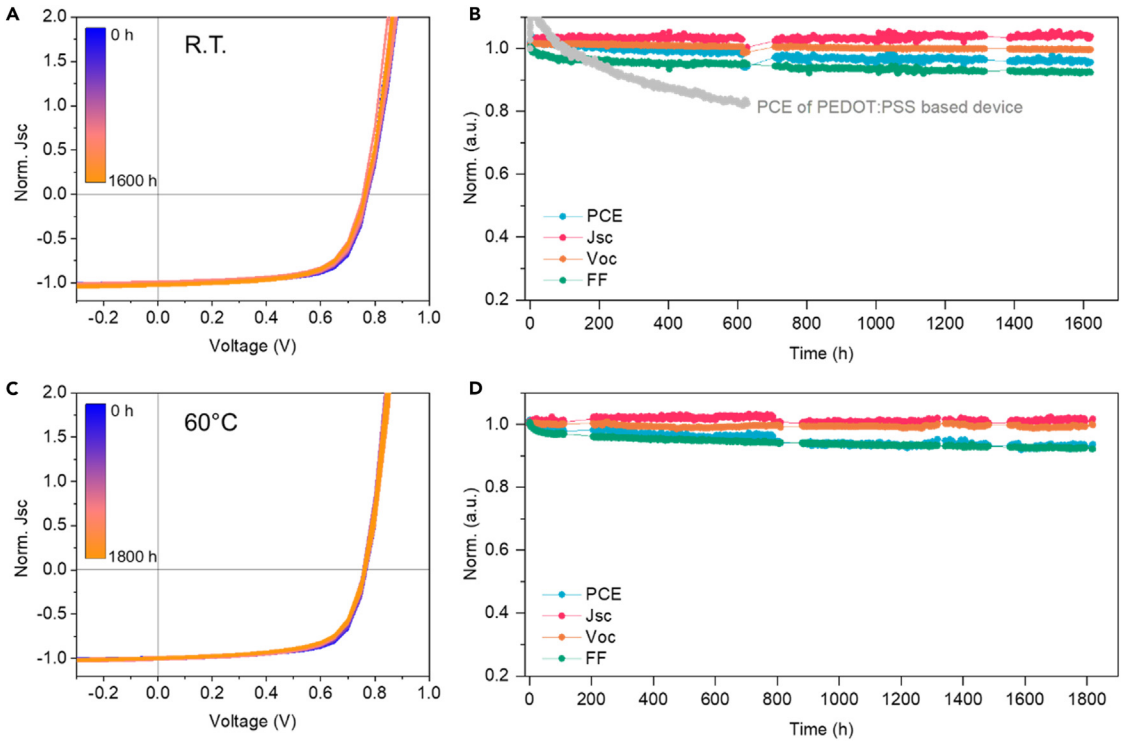

Figure 3. Operational stability of bilayer HTL-based OPV cells

(A and C) J-V curves of unencapsulated bilayer devices aged at RT (A) and 60°C (C) in a N_2-filled chamber under metal-halide lamps with UV filters. (B and D) Normalized photovoltaic parameters extracted from (A) and (C), respectively. For comparison, the evolution of the PV parameters for a device with a PEDOT:PSS only HTL is depicted in gray in (B).

phenomenon is not further investigated in the present work, we want to note that Torres-Herrera has suggested the limited conductivity of ev-MoO_x as a possible cause for such small losses.[38] Additionally, we studied the long-term stability of these devices based on different active layers and HTLs. As expected, the normalized PCE of the bilayer devices is more stable than for any other HTL combination. The D-PTAAnp/PEDOT:PSS bilayer devices maintained approximately 94%, 82%, 90%, and 93% of their initial values for PM7:Y6, PTQ11:Y6, PM6:DT-Y6, and PM6:BTP-eC9:L8-BO after 600 h operation, respectively. The corresponding systems based on ev-MoO_x preserved 85%, 72%, 81%, and 85%, respectively. By contrast, the control devices based on PEDOT:PSS declined rapidly within the first 200 h. The relatively stable PCE of bilayer devices reveals that better interfacial contact between the active layer and the electrode is crucial for achieving long-term stability.

All-solution-processed OPV cells

To achieve all-solution-processed OPV cells, the evaporated silver electrode was replaced by AgNWs. The device architecture for which the AgNWs were doctor-bladed in ambient atmosphere is shown in Figure 5A. Because of the high transmittance of the bilayer HTL and the AgNW electrode, the total transmittance of the whole device stack is relatively high. An average transmission value of 30% is measured for the spectral regime between 400 and 800 nm, as shown in Figure S26. Such values are already interesting for window applications.[39] The devices provide a PCE of 8.23%, with a J_{sc} of 14.72 mA/cm^2, a V_{oc} of 0.81 V, and a FF of 68.7% when illuminating from the front of the device. In order to reflect the transmitted photons

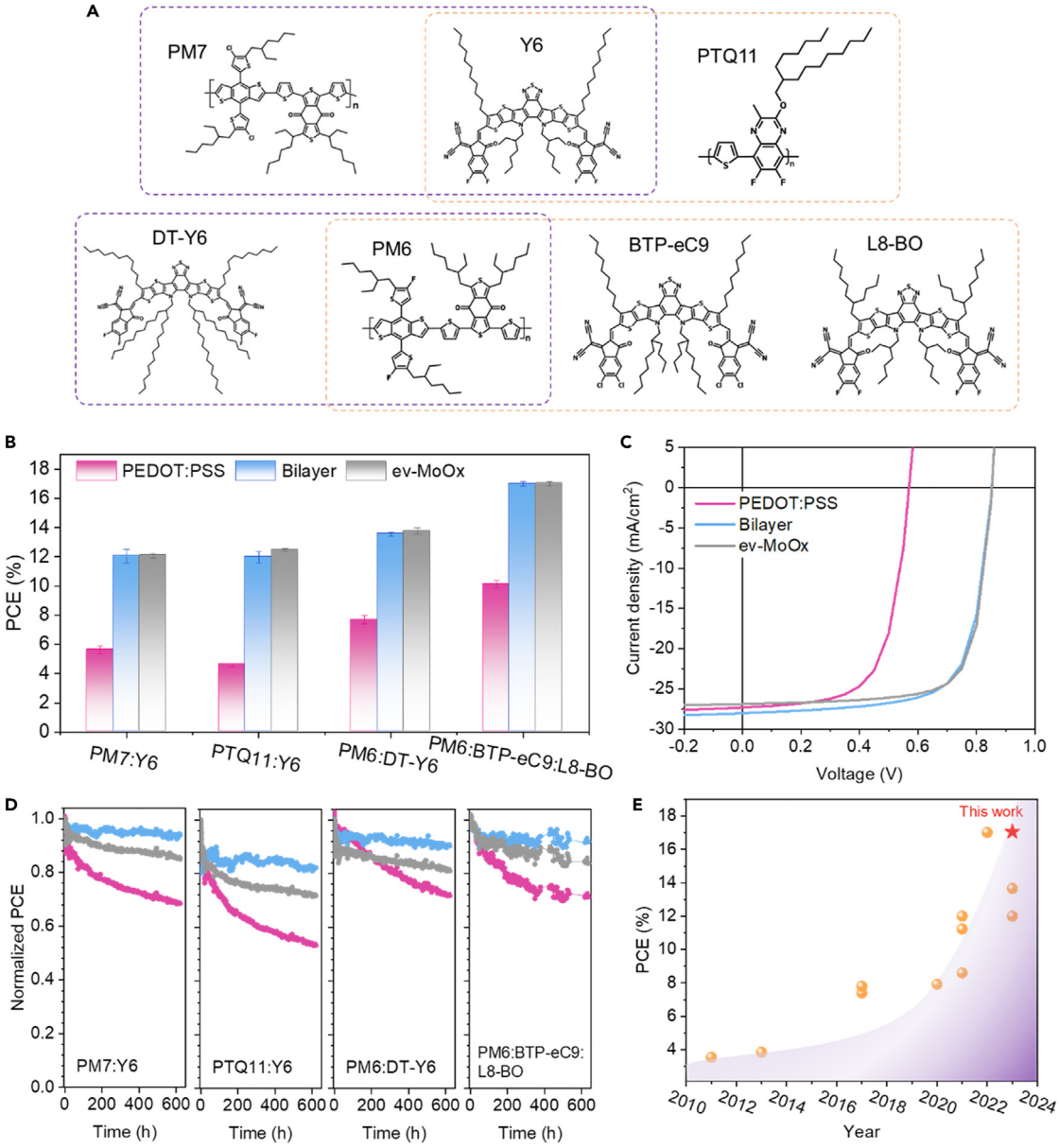

Figure 4. Universality of the bilayer HTL in OPV cells

(A) Chemical structures of polymer donors and acceptors for universality test.

(B) PCE of OPV cells based on various active layer systems using different HTLs. Average values were obtained from over 6 devices. Error bars represent standard deviations.

(C) J-V characteristics of PM6:BTP-eC9:L8-BO-based devices.

(D) Long-term stability (at RT in a N_2 filled chamber under metal-halide lamps with UV filters) of the different OPV cells.

(E) PCE evolution of inverted OPV cells with solution-processed HTL. The photovoltaic data and corresponding references are included in Table S5.

back into the device and make the device more comparable to devices with evaporated silver, a mirror was placed behind the back electrode. The J_{sc} was increased to 17.37 mA/cm^2, resulting in a PCE of 9.46% (Figure 5C). EQE measurements confirmed the enhanced J_{sc} values (Figure 5D). This indicates that besides absorption losses in the semitransparent device, there are some small additional losses related to the AgNW processing. In addition, we checked the operation stability of unencapsulated AgNWs devices at RT in N_2, following the ISOS-L-1 protocol.

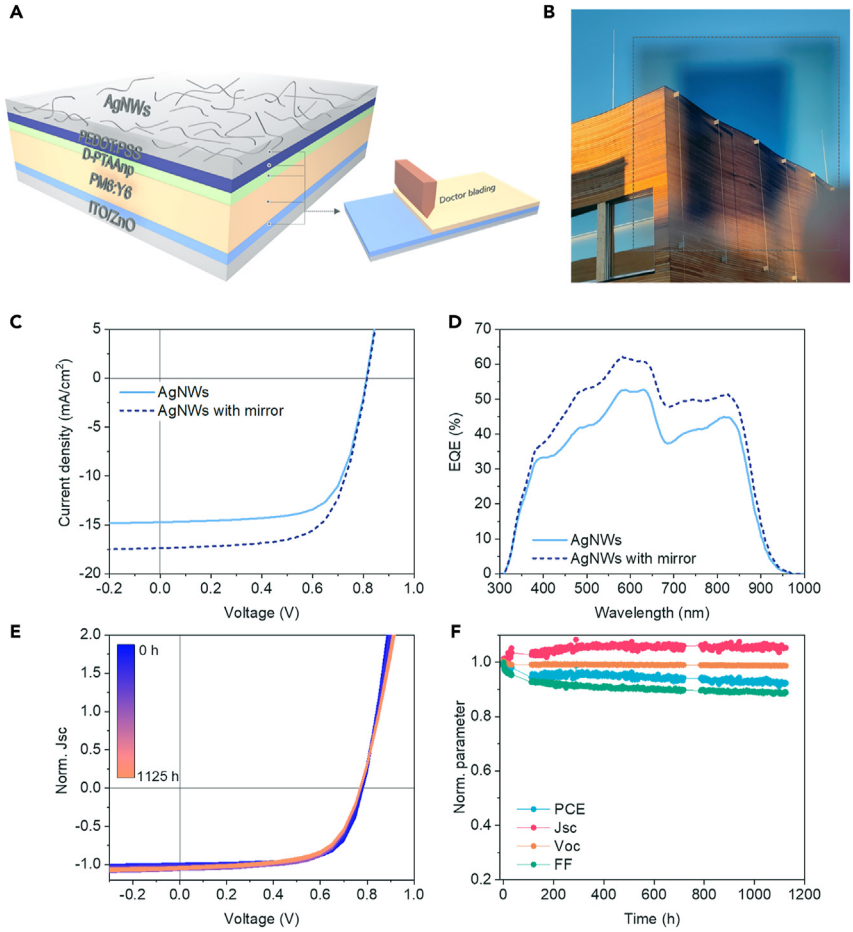

Figure 5. Performance of all-solution-processed OPV cells based on bilayer HTL

(A) Scheme of all-solution-processed OPV cells based on bilayer HTL with AgNWs as top electrode. Each layer was doctor-bladed in ambient atmosphere.

(B) Photograph of all-solution-processed OPV cells on an ITO substrate.

(C and D) (C) J-V characteristics and (D) EQE spectra of OPV cells, illuminating from the front of the device with (dashed lines) or without (solid lines) reflecting mirror in the back.

(E) J-V curves of all-solution-processed OPV cells aged at RT in a N_2 filled chamber under metal-halide lamps with UV filters.

(F) Normalized photovoltaic parameters extracted from (E).

The AgNW-based devices maintain 92% of their initial efficiency after 1,100 h of operation, whereas the PCE of the control device (with only PEDOT:PSS on top of the active layer) decreased by 40% in the first 200 h (Figure S27).

A printed electrode can be fabricated using techniques such as screen printing or inkjet printing in large-scale production. Motivated that printed electrodes require crosslinked PEDOT:PSS, we further performed crosslinking treatment on PEDOT:PSS, and its effect on device photovoltaic performance and stability was investigated in detail. The crosslinked device achieved a performance of 13.47%, along with a slight decrease in FF compared with the one of the uncrosslinked device (Figure S28). This is probably due to the relatively lower electrical conductivity of PEDOT:PSS layer after crosslink treatment. The concentration of the crosslinking agent is 0.15 vol %, which was optimized in our previous study.[40] Further modifications on PEDOT:PSS thickness and crosslinking agent concentrations would overcome the large series resistance in the device and

improve the performance to some extent. As can be seen in Figure S29, the AgNWs device based on crosslinked PEDOT:PSS shows a respectable stability, maintaining 85% of the initial PCE for 1,100 h. However, we also observe that the crosslinking agents do cause an instant efficiency drop during operation when the concentration goes higher and operational temperature increases (60°C, Figure S30). This would limit the applicability of the device at elevated temperature operating conditions, even if good photovoltaic performance and stability are attained at RT. The residual crosslinking agent probably induces further reaction at elevated temperatures, which causes the charge carriers transport problem and adversely affects device stability. Nevertheless, we believe that our architecture offers all the versatility required to overcome that. For instance, preliminary trials with a triple interface layer showed that crosslinked PEDOT:PSS can be processed on Al 4083 PEDOT:PSS, with no significant losses in FF (Figure S31). Further studies with screen-printed Ag electrodes would be interesting to undertake.

Conclusions

We introduce a novel device architecture for highly efficient and stable NFA-based OPV cells that is capable to operate with conventional acidic PEDOT:PSS in a solution-processed bilayer polymer as an HTL. Through a rational interface design, sandwiching D-PTAAnp layer between the active layer and PEDOT:PSS, a robust interlayer is established, enabling proper alignment of the hole transport levels, overall low contact resistance, and a continuous coating of aqueous PEDOT:PSS without any surfactant. We have explored HTL with various active layers and with various ETLs, compared it with multiple other HTL systems, and consistently always found equal or better efficiency and significantly improved stability. Particularly, the inverted OPV cells based on PM6:BTP-eC9:L8-BO achieve an outstanding PCE of 17.1%. The devices also exhibit excellent operational stability and retain 95% of their initial performance after 1,600 h operating under metal-halide lamp illumination at RT and 93% of their initial performance after 1,800 h operating under metal-halide lamp illumination at 60°C. We further demonstrate all-solution-processed devices based on AgNWs electrode with impressive efficiency and stability. Overall, the performance and stability values achieved while including a solution-processed top PEDOT:PSS layer present a key enabling tool toward industrially scalable PM6:Y6 modules.

EXPERIMENTAL PROCEDURES

Resource availability

Lead contact

Further information and requests for resources should be directed to and will be fulfilled by the lead contact, Thomas Heumüller (thomas.heumueller@fau.de).

Materials availability

This study did not generate new, unique materials.

Data and code availability

All the data supporting the findings of this study are presented in the paper and in the supplemental information. This study did not generate or analyze datasets or code.

Materials

Poly[(2,6-(4,8-bis(5-(2-ethylhexyl-3-fluoro)thiophen-2-yl)-benzo[1,2-b:4,5 b′]dithiophene))-alt-(5,5-(1′,3′-di-2-thienyl-5′,7′-bis(2-ethylhexyl)benzo[1′,2′-c:4′,5′-c′]dithiophene-4,8-dione)], PM6, poly[(2,6-(4,8-bis(5-(2-ethylhexyl-3-chloro)thiophen-2-yl)-benzo[1,2-b:4,5-b′]dithiophene))-alt-(5,5-(1′,3′-di-2-thienyl-5′,7′-bis(2-ethylhexyl)

benzo[1′,2′-c:4′,5′-c′]dithiophene-4,8-dione)], PM7 and 2,2′-((2Z,2′Z)-((12,13-bis(2-ethylhexyl)-3,9-diundecyl-12,13-dihydro-[1,2,5]thiadiazolo[3,4-e]thieno[2″,3″:4′,5′]thieno[2′,3′:4,5]pyrrolo[3,2-g]thieno[2′,3′:4,5]thieno[3,2-b]indole-2,10-diyl)bis(methanylylidene))bis(5,6-difluoro-3-oxo-2,3-dihydro-1H-indene-2,1-diylidene))dimalononitrile, Y6, 2,2′-[[12,13-bis(2-butyloctyl)-12,13-dihydro-3,9-dinonylbisthieno[2″,3″:4′,5′]thieno[2′,3′:4,5]pyrrolo[3,2-e:2′,3′-g][2,1,3]benzothiadiazole-2,10-diyl]bis[methylidyne(5,6-chloro-3-oxo-1H-indene-2,1(3H)-diylidene)]]bis[propanedinitrile], BTP-eC9, 2,2′-((2Z,2′Z)-((12,13-bis(2-ethylhexyl)-3,9-(2-butyloctyl)-12,13-dihydro-[1,2,5]thiadiazolo[3,4-e]thieno[2″,3″:4′,5′]thieno[2′,3′:4,5]pyrrolo[3,2-g]thieno[2′,3′:4,5]thieno[3,2-b]indole-2,10-diyl)bis(methanylylidene))bis(5,6-difluoro-3-oxo-2,3-dihydro-1H-indene-2,1-diylidene))dimalononitrile, L8-BO were purchased from Solarmer Materials. Poly[(thiophene)-alt-(6,7-difluoro-2-(2-hexyldecyloxy)-3-methylquinoxaline], and PTQ11 was purchased from 1-Material. 2,2′-((2Z,2′Z)-((12,13-bis(2-decylteradecyl)-3,9-diundecyl-12,13-dihydro-[1,2,5]thiadiazolo[3,4-e]thieno[2″,3″:4′,5′]thieno[2′,3′:4,5]pyrrolo[3,2-g]thieno[2′,3′:4,5]thieno[3,2-b]indole-2,10-diyl)bis(methanylylidene))bis(5,6-difluoro-3-oxo-2,3-dihydro-1H-indene-2,1-diylidene))dimalononitrile, DT-Y6 was offered by Prof. Fei Huang group. All the materials were used as received without further purification. Lewis acid dopant tris(pentafluorophenyl)-borane is from TCI. ZnO, Ta-WO_x, and Sb-SnO_x nanoparticle dispersions were purchased from Avantama. MoO_x nanoparticle dispersion was received from Nanograde. (3-Glycidyloxypropyl)trimethoxysilane (GOPS) was purchased from Aldrich. AgNWs ink (dispersed in alcohol) was received from Cambrios Technology Corporation.

Device fabrication

The OPV cells were fabricated in an inverted structure of ITO/ETL/active layer/HTL/Ag. The ITO-coated glass substrates were cleaned with acetone and isopropanol in an ultrasonic bath for 10 min each. After drying, ZnO sol-gel solution was spin-coated on the ITO substrates, and baked at 200°C for 20 min under ambient condition. ZnO sol-gel solution was prepared according to the literature.[41] The same procedure was applied to the commercial ZnO nanoparticle dispersion. The substrates were then transferred into a nitrogen-filled glove box. Subsequently, a mixed solution of PM6:Y6 (1:1.2, wt %) with 16 mg/mL in chloroform was spin-coated onto the ZnO layer. The other three active layers, PM7:Y6 (16 mg/mL in chloroform), PTQ11:Y6 (16 mg/mL in chloroform), PM6:DT-Y6 (20 mg/mL in xylene), and PM6:BTP-eC9:L8-BO (16 mg/mL in chloroform) with various weight ratios were spin-coated on top of the ZnO layer. The additives were 0.5% chloronaphthalene (CN) for PM6:Y6 and PM7:Y6 and 0.5% diiodomethane (DIM) for PM6:BTP-eC9:L8-BO. The D-PTAAnp dispersion was synthesized according to our previously published procedure. PTAA (8 mg) with 10 wt % LAD dopant was dissolved in chloroform (1 mL) and injected into isopropanol (4 mL) under vigorous stirring. N_2 gas was used to remove chloroform, resulting in a final dispersion concentration of 4 mg/ml doped polymer NP. For the development of bilayer architecture, D-PTAAnp dispersion was doctor-bladed on the active layer. Subsequently, PEDOT:PSS (Clevios, AI 4083, diluted with isopropanol) was doctor-bladed with the substrate temperature kept at 65°C. Then, the substrate was annealed at 110°C for 5 min in the glovebox. The crosslinked PEDOT:PSS was mixed with GOPS (a hydrolyzed silane crosslinker) at a concentration of 0.15 vol %. For the control device, PEDOT:PSS was diluted in isopropanol (1:5 vol %, 0.13 wt % Dynol in isopropanol to improve wettability on top of the active layer). Finally, Ag electrode (100 nm) was thermally evaporated through a mask (10.4 mm^2 active area opening) under a vacuum of approximately 1×10^{-6} mbar. For the all-solution-processed device, ZnO and bilayer HTL were prepared following the same procedure on an ITO patterned substrate. PM6:Y6 (16 mg/mL in chloroform) was

doctor-bladed on top of ZnO layer with a 150 μm gap between substrate and blade at 30°C. The AgNWs layer was doctor-bladed on top of the active layer and annealed at 130°C for 3 min in the glovebox.

Device characterization

The devices were measured under one-sun illumination using a solar cell simulator (AM 1.5 global spectrum with 100 mW/cm^2 intensity calibrated using a silicon reference diode). The J-V characteristics were recorded using a source measure unit Keysight B2901A between −0.3 and +1 V at scanning increments of 50 mV. The EQE data were acquired with monochromatic light using an integrated system from Enlitech. All the measurements were tested in ambient air. The particle size and distribution spectrum were recorded by dynamic light scattering (DLS) on a Microtrac NANO-flex at RT. UV-vis absorption measurements were performed on a PerkinElmer Lambda 950 spectrometer. Kelvin probe measurements were carried out on a KP technology single point system. Conductivity measurement of nanoparticle films was performed on ITO interdigitated substrates. The contact angles of the films were measured using Dataphysics OCA 20. SEM images were obtained using FEI Sirion SEM at 1 kV accelerating voltage. AFM measurements were performed with a Nanosurf Easy Scan 2 in tapping mode. The average visible transmission (AVT) value of the full-solution-processed device can be calculated according to the following equation:

$$\mathrm{AVT} = \frac{\int T(\lambda)P(\lambda)S(\lambda)d(\lambda)}{\int P(\lambda)S(\lambda)d(\lambda)}$$

Where λ is the wavelength, T(λ) is the transmission of the device, P(λ) is the photopic response of the human eyes, S(λ) is the solar photon flux in AM1.5G

Device stability measurement

All the devices were kept in a home-built chamber in an N_2 atmosphere with a UV filter (cutoff 380 nm, the light spectrum is shown in Figure S32). The photovoltaic characteristics of the devices under metal-halide lamps were recorded by using a source measurement unit Keysight B2901A, and the efficiency monitoring system was periodically operated by a program designed in our lab. For stability measurements at RT (following ISOS-L-1 protocol, 1 Sun illumination at RT), the chamber was equipped with a cooling system that maintained the temperature at around 35°C as monitored by a thermocouple. For stability measurements at 60°C (following ISOS-L-2 protocol, 1 Sun illumination at 65°C), a hot plate beneath the chamber controlled the temperature. However, the recorded temperature is around 60°C probably due to the location of the thermocouple in the chamber.

UPS

UPS measurements of the SECO and the HOMO regions of PM6:Y6, PM6:Y6/PEDOT:PSS, and PM6:Y6/D-PTAAnp/PEDOT:PSS bilayer HTL samples were conducted with a ScientaOmicron Argus CU electron analyzer and He I (21.1 eV) excitation, using a Prevac UVS 40A2 gas discharge lamp. For these measurements, a pass energy of 5 eV was used. Work function (Φ) and HOMO values were determined by linear extrapolation of the SECO and leading edge of the HOMO spectrum, respectively. The kinetic energy (KE) of photoelectrons derived from these energy regions is ∼20 eV. Based on the "universal curve" of electron inelastic mean free path (IMFP) as a function of KE,[42] the exponentially decreasing information depth (ID, taken as 3 × IMFP) of these measurements is estimated to be ∼2–3 nm. The energy scale of the UPS spectra is referenced to the Fermi edge (E_F) of a sputter-cleaned Au foil.

SUPPLEMENTAL INFORMATION

Supplemental information can be found online at https://doi.org/10.1016/j.joule.2024.06.013.

ACKNOWLEDGMENTS

J.X. acknowledges the support from the China Scholarship Council (CSC). V.M.L.C. acknowledges the support of the H2020 European project Citysolar, grant agreement number 101007084. R.F., J.F., and M.B. are grateful to the Energy Materials *In Situ* Laboratory (EMIL) at HZB for providing access to analytical infrastructure. T.H. and C.J.B. gratefully acknowledge the Deutsche Forschungsgemeinschaft (DFG) for financial support in scope of the SFB 953 (182849149), as well as within the Popular project under grant agreement 461909888, "ELF-PV - Design and development of solution-processed functional materials for the next generations of PV technologies" (no. 44-6521a/20/4), Solar TAP—a Technology Acceleration Platform for emerging Photovoltaics, the "Aufbruch Bayern" initiative of the state of Bavaria (EnCN and SFF), and the European Union's Horizon 2020 research and innovation program under grant agreement no. 952911 (BOOSTER) and 101137889 (PH2OTOGEN).

AUTHOR CONTRIBUTIONS

J.X., T.H., and C.J.B. conceived the idea. J.X. carried out the device fabrication experiments, characterizations, and data analysis. V.M.L.C. conducted drift-diffusion simulation of the devices. A.B. conducted the SEM measurement. R.F. and J.F. conducted the UPS measurement. J.X. wrote the original draft manuscript. R.F., M.B., and C.J.B. revised the manuscript. All authors discussed and commented on the manuscript.

DECLARATION OF INTERESTS

The authors declare no competing interests.

Received: January 24, 2024
Revised: April 5, 2024
Accepted: June 17, 2024
Published: July 9, 2024

REFERENCES

1. Kaltenbrunner, M., White, M.S., Głowacki, E.D., Sekitani, T., Someya, T., Sariciftci, N.S., and Bauer, S. (2012). Ultrathin and lightweight organic solar cells with high flexibility. Nat. Commun. *3*, 770. https://doi.org/10.1038/ncomms1772.

2. Jinno, H., Fukuda, K., Xu, X., Park, S., Suzuki, Y., Koizumi, M., Yokota, T., Osaka, I., Takimiya, K., and Someya, T. (2017). Stretchable and waterproof elastomer-coated organic photovoltaics for washable electronic textile applications. Nat. Energy *2*, 780–785. https://doi.org/10.1038/s41560-017-0001-3.

3. Xu, X., Fukuda, K., Karki, A., Park, S., Kimura, H., Jinno, H., Watanabe, N., Yamamoto, S., Shimomura, S., Kitazawa, D., et al. (2018). Thermally stable, highly efficient, ultraflexible organic photovoltaics. Proc. Natl. Acad. Sci. USA *115*, 4589–4594. https://doi.org/10.1073/pnas.1801187115.

4. Distler, A., Brabec, C.J., and Egelhaaf, H.J. (2021). Organic photovoltaic modules with new world record efficiencies. Prog. Photovolt. Res. Appl. *29*, 24–31. https://doi.org/10.1002/pip.3336.

5. Hou, J., Inganäs, O., Friend, R.H., and Gao, F. (2018). Organic solar cells based on non-fullerene acceptors. Nat. Mater. *17*, 119–128. https://doi.org/10.1038/nmat5063.

6. Zhang, G., Zhao, J., Chow, P.C.Y., Jiang, K., Zhang, J., Zhu, Z., Zhang, J., Huang, F., and Yan, H. (2018). Nonfullerene Acceptor Molecules for Bulk Heterojunction Organic Solar Cells. Chem. Rev. *118*, 3447–3507. https://doi.org/10.1021/acs.chemrev.7b00535.

7. Yuan, J., Zhang, Y., Zhou, L., Zhang, G., Yip, H.L., Lau, T.K., Lu, X., Zhu, C., Peng, H., Johnson, P.A., et al. (2019). Single-Junction Organic Solar Cell with over 15% Efficiency Using Fused-Ring Acceptor with Electron-Deficient Core. Joule *3*, 1140–1151. https://doi.org/10.1016/j.joule.2019.01.004.

8. Liu, Q., Jiang, Y., Jin, K., Qin, J., Xu, J., Li, W., Xiong, J., Liu, J., Xiao, Z., Sun, K., et al. (2020). 18% Efficiency organic solar cells. Sci. Bull. *65*, 272–275. https://doi.org/10.1016/j.scib.2020.01.001.

9. Li, C., Zhou, J., Song, J., Xu, J., Zhang, H., Zhang, X., Guo, J., Zhu, L., Wei, D., Han, G., et al. (2021). Non-fullerene acceptors with branched side chains and improved molecular packing to exceed 18% efficiency in organic solar cells. Nat. Energy *6*, 605–613. https://doi.org/10.1038/s41560-021-00820-x.

10. Mateker, W.R., and McGehee, M.D. (2017). Progress in Understanding Degradation Mechanisms and Improving Stability in Organic Photovoltaics. Adv. Mater. *29*, 1603940. https://doi.org/10.1002/adma.201603940.

11. Li, N., Perea, J.D., Kassar, T., Richter, M., Heumueller, T., Matt, G.J., Hou, Y., Güldal, N.S., Chen, H., Chen, S., et al. (2017). Abnormal strong burn-in degradation of highly efficient polymer solar cells caused by spinodal donor-acceptor demixing. Nat. Commun. *8*, 14541.

12. Zhang, C., Heumueller, T., Leon, S., Gruber, W., Burlafinger, K., Tang, X., Perea, J.D., Wabra, I., Hirsch, A., Unruh, T., et al. (2019). A top-down strategy identifying molecular phase stabilizers to overcome microstructure instabilities in organic solar cells. Energy Environ. Sci. *12*, 1078–1087. https://doi.org/10.1039/C8EE03780A.

13. Gasparini, N., Salvador, M., Strohm, S., Heumueller, T., Levchuk, I., Wadsworth, A., Bannock, J.H., de Mello, J.C., Egelhaaf, H.J., Baran, D., et al. (2017). Burn-in free nonfullerene-based organic solar cells. Adv. Energy Mater. *7*, 1700770. https://doi.org/10.1002/aenm.201700770.

14. Cha, H., Wu, J., Wadsworth, A., Nagitta, J., Limbu, S., Pont, S., Li, Z., Searle, J., Wyatt, M.F., Baran, D., et al. (2017). An Efficient, "Burn in" Free Organic Solar Cell Employing a Nonfullerene Electron Acceptor. Adv. Mater. *29*, 1701156. https://doi.org/10.1002/adma.201701156.

15. Heumueller, T., Mateker, W.R., Sachs-Quintana, I.T., Vandewal, K., Bartelt, J.A., Burke, T.M., Ameri, T., Brabec, C.J., and McGehee, M.D. (2014). Reducing burn-in voltage loss in polymer solar cells by increasing the polymer crystallinity. Energy Environ. Sci. *7*, 2974–2980. https://doi.org/10.1039/C4EE01842G.

16. Heumueller, T., Burke, T.M., Mateker, W.R., Sachs-Quintana, I.T., Vandewal, K., Brabec, C.J., and McGehee, M.D. (2015). Disorder-Induced Open-Circuit Voltage Losses in Organic Solar Cells during Photoinduced Burn-In. Adv. Energy Mater. *5*, 1500111.

17. Ghasemi, M., Balar, N., Peng, Z., Hu, H., Qin, Y., Kim, T., Rech, J.J., Bidwell, M., Mask, W., McCulloch, I., et al. (2021). A molecular interaction–diffusion framework for predicting organic solar cell stability. Nat. Mater. *20*, 525–532. https://doi.org/10.1038/s41563-020-00872-6.

18. Gasparini, N., Paleti, S.H.K., Bertrandie, J., Cai, G., Zhang, G., Wadsworth, A., Lu, X., Yip, H.-L., McCulloch, I., and Baran, D. (2020). Exploiting Ternary Blends for Improved Photostability in High-Efficiency Organic Solar Cells. ACS Energy Lett. *5*, 1371–1379. https://doi.org/10.1021/acsenergylett.0c00604.

19. Chen, H., Zhang, R., Chen, X., Zeng, G., Kobera, L., Abbrent, S., Zhang, B., Chen, W., Xu, G., Oh, J., et al. (2021). A guest-assisted molecular-organization approach for >17% efficiency organic solar cells using environmentally friendly solvents. Nat. Energy *6*, 1045–1053. https://doi.org/10.1038/s41560-021-00923-5.

20. Sun, R., Wang, W., Yu, H., Chen, Z., Xia, X.X., Shen, H., Guo, J., Shi, M., Zheng, Y., Wu, Y., et al. (2021). Achieving over 17% efficiency of ternary all-polymer solar cells with two well-compatible polymer acceptors. Joule *5*, 1548–1565. https://doi.org/10.1016/j.joule.2021.04.007.

21. Yang, W., Luo, Z., Sun, R., Guo, J., Wang, T., Wu, Y., Wang, W., Guo, J., Wu, Q., Shi, M., et al. (2020). Simultaneous enhanced efficiency and thermal stability in organic solar cells from a polymer acceptor additive. Nat. Commun. *11*, 1218. https://doi.org/10.1038/s41467-020-14926-5.

22. Li, Y., Huang, X., Ding, K., Sheriff, K.M., Ade, H., Forrest, S.R., Ye, L., Liu, H., and Li, C. (2021). Non-fullerene acceptor organic photovoltaics with intrinsic operational lifetimes over 30 years. Nat. Commun. *12*, 5419.

23. Hu, H., Ghasemi, M., Peng, Z., Zhang, J., Rech, J.J., You, W., Yan, H., and Ade, H. (2020). The Role of Demixing and Crystallization Kinetics on the Stability of Non-Fullerene Organic Solar Cells. Adv. Mater. *32*, e2005348. https://doi.org/10.1002/adma.202005348.

24. Guo, F., Zhu, X., Forberich, K., Krantz, J., Stubhan, T., Salinas, M., Halik, M., Spallek, S., Butz, B., Spiecker, E., et al. (2013). ITO-free and fully solution-processed semitransparent organic solar cells with high fill factors. Adv. Energy Mater. *3*, 1062–1067. https://doi.org/10.1002/aenm.201300100.

25. Czolk, J., Landerer, D., Koppitz, M., Nass, D., and Colsmann, A. (2016). Highly Efficient, Mechanically Flexible, Semi-Transparent Organic Solar Cells Doctor Bladed from Non-Halogenated Solvents. Adv. Mater. Technol. *1*, 1600184. https://doi.org/10.1002/admt.201600184.

26. Lucera, L., Machui, F., Schmidt, H.D., Ahmad, T., Kubis, P., Strohm, S., Hepp, J., Vetter, A., Egelhaaf, H.J., and Brabec, C.J. (2017). Printed semi-transparent large area organic photovoltaic modules with power conversion efficiencies of close to 5 %. Org. Electron. *45*, 209–214. https://doi.org/10.1016/j.orgel.2017.03.013.

27. Kamoun, O., Gassoumi, A., Kouass, S., Alhalaili, B., Vidu, R., and Turki-Kamoun, N. (2020). An Investigation on the Synthesis of Molybdenum Oxide and Its Silica Nanoparticle Composites for Dye Degradation. Nanomaterials (Basel) *10*, 2409. https://doi.org/10.3390/nano10122409.

28. Kusoglu, A., and Weber, A.Z. (2017). New Insights into Perfluorinated Sulfonic-Acid Ionomers. Chem. Rev. *117*, 987–1104. https://doi.org/10.1021/acs.chemrev.6b00159.

29. Jiang, Y., Dong, X., Sun, L., Liu, T., Qin, F., Xie, C., Jiang, P., Hu, L., Lu, X., Zhou, X., et al. (2022). An alcohol-dispersed conducting polymer complex for fully printable organic solar cells with improved stability. Nat. Energy *7*, 352–359. https://doi.org/10.1038/s41560-022-00997-9.

30. Xu, J., Späth, A., Gruber, W., Barabash, A., Stadler, P., Gubanov, K., Wu, M., Forberich, K., Spiecker, E., Fink, R.H., et al. (2023). Tailoring doped organic nanoparticles as selective hole transporters for printed non-fullerene organic solar cells. Nano Energy *118*, 108956. https://doi.org/10.1016/j.nanoen.2023.108956.

31. Han, Y.W., Jeon, S.J., Lee, H.S., Park, H., Kim, K.S., Lee, H.-W., and Moon, D.K. (2019). Evaporation-Free Nonfullerene Flexible Organic Solar Cell Modules Manufactured by An All-Solution Process. Adv. Energy Mater. *9*, 1902065. https://doi.org/10.1002/aenm.201902065.

32. Hou, Y., Xie, C., Radmilovic, V.V., Puscher, B., Wu, M., Heumüller, T., Karl, A., Li, N., Tang, X., Meng, W., et al. (2019). Assembling Mesoscale-Structured Organic Interfaces in Perovskite Photovoltaics. Adv. Mater. *31*, e1806516. https://doi.org/10.1002/adma.201806516.

33. Ye, T., Chen, W., Jin, S., Hao, S., Zhang, X., Liu, H., and He, D. (2019). Enhanced Efficiency of Planar Heterojunction Perovskite Solar Cells by a Light Soaking Treatment on Tris(pentafluorophenyl)borane-Doped Poly(triarylamine) Solution. ACS Appl. Mater. Interfaces *11*, 14004–14010. https://doi.org/10.1021/acsami.8b18663.

34. Röhr, J.A. (2019). Direct Determination of Built-in Voltages in Asymmetric Single-Carrier Devices. Phys. Rev. Appl. *11*, 054079. https://doi.org/10.1103/PhysRevApplied.11.054079.

35. Le Corre, V.M., Duijnstee, E.A., El Tambouli, O., Ball, J.M., Snaith, H.J., Lim, J., and Koster, L.J.A. (2021). Revealing Charge Carrier Mobility and Defect Densities in Metal Halide Perovskites via Space-Charge-Limited Current Measurements. ACS Energy Lett. *6*, 1087–1094. https://doi.org/10.1021/acsenergylett.0c02599.

36. Bubnova, O., Khan, Z.U., Wang, H., Braun, S., Evans, D.R., Fabretto, M., Hojati-Talemi, P., Dagnelund, D., Arlin, J.B., Geerts, Y.H., et al. (2014). Semi-metallic polymers. Nat. Mater. *13*, 190–194. https://doi.org/10.1038/nmat3824.

37. Sun, L., Zeng, W., Xie, C., Hu, L., Dong, X., Qin, F., Wang, W., Liu, T., Jiang, X., Jiang, Y., et al. (2020). Flexible All-Solution-Processed Organic Solar Cells with High-Performance Nonfullerene Active Layers. Adv. Mater. *32*, e1907840. https://doi.org/10.1002/adma.201907840.

38. Torres-Herrera, D.M., Moreno-Romero, P.M., Cabrera-German, D., Cortina-Marrero, H.J., Sotelo-Lerma, M., and Hu, H. (2020). Thermal co-evaporated MoOx:Au thin films and its application as anode modifier in perovskite solar cells. Sol. Energy *206*, 136–144. https://doi.org/10.1016/j.solener.2020.05.105.

39. Chen, K.S., Salinas, J.F., Yip, H.L., Huo, L., Hou, J., and Jen, A.K.Y. (2012). Semi-transparent polymer solar cells with 6% PCE, 25% average visible transmittance and a color rendering index close to 100 for power generating window applications. Energy Environ. Sci. *5*, 9551–9557. https://doi.org/10.1039/c2ee22623e.

40. Liu, C., Du, X., Gao, S., Classen, A., Osvet, A., He, Y., Mayrhofer, K., Li, N., and Brabec, C.J. (2020). A Cross-Linked Interconnecting Layer Enabling Reliable and Reproducible Solution-Processing of Organic Tandem Solar Cells. Adv. Energy Mater. *10*, 1903800. https://doi.org/10.1002/aenm.201903800.

41. Qin, F., Wang, W., Sun, L., Jiang, X., Hu, L., Xiong, S., Liu, T., Dong, X., Li, J., Jiang, Y., et al. (2020). Robust metal ion-chelated polymer interfacial layer for ultraflexible non-fullerene organic solar cells. Nat. Commun. *11*, 4508.

42. Seah, M.P., and Dench, W.A. (1979). Quantitative electron spectroscopy of surfaces: A standard data base for electron inelastic mean free paths in solids. Surf. Interface Anal. *1*, 2–11. https://doi.org/10.1002/sia.740010103.